Characterization of Linear Viscoelastic Behavior of Epoxy Molding Compound Subjected to Uniaxial Compression and Hydrostatic Pressure

Hyun Seop Lee, Yong Sun, Changsu Kim, and Bongtae Han

***Abstract*— The linear viscoelastic properties of epoxy molding compound (EMC) are measured by an embedded fiber Bragg grating (FBG) sensor. A single cylindrical EMC specimen is fabricated, and it is subjected to constant uniaxial compression and hydrostatic pressure at various temperatures. The FBG embedded in the specimen records strain histories as a function of time. Two linear viscoelastic properties (Young's modulus and bulk modulus) are determined from the strain histories. The master curves of two properties are produced, and the corresponding shift factors are determined using a piecewise function. The validity of three major assumptions associated with the linear viscoelasticity—thermorheological simplicity, Boltzmann superposition, and linearity—is verified by supplementary experiments. The accuracy of the measured properties is corroborated by the warpage measurement of a bimaterial specimen subjected to a temperature cycle. The effect of the time-dependent bulk modulus on the warpage is also discussed.**

***Index Terms*— Bulk modulus, epoxy molding compound (EMC), hydrostatic pressure, linear viscoelasticity, master curve, shift function, uniaxial compression, warpage prediction, Young's modulus.**

I. Introduction

EPOXY molding compound (EMC) is a thermosetting polymer filled with inorganic fillers such as fused silica. EMC has been used extensively as a protection layer in various semiconductor packages. The warpage and the residual stress of packages are directly related to the thermomechanical properties of EMC. As the size of the semiconductor packages continues to shrink, the prediction of the warpage and residual stress becomes increasingly important [1]–[3]. The viscoelastic properties of EMC are the most critical input data required for accurate prediction.

The constitutive law of the linear viscoelasticity is [4]

$$s_{ij}(t) = 2\int G(t-\tau)\frac{\partial e_{ij}(\tau)}{\partial \tau}d\tau$$
$$\sigma_{kk}(t) = 3\int K(t-\tau)\frac{\partial \varepsilon_{kk}(\tau)}{\partial \tau}d\tau \quad (1)$$

where s_{ij} and e_{ij} are the deviatoric stress and strain tensors, respectively, $G(t)$ and $K(t)$ are the time-dependent shear modulus and bulk modulus, respectively, and σ_{kk} and ε_{kk} are the dilatational stress and strain tensors, respectively.

In the linear viscoelasticity regime, two elastic constants in (1) have the following relationships with two other elastic constants as [5]:

$$K(t) = \frac{E(t)G(t)}{9G(t) - 3E(t)}, \quad G(t) = \frac{E(t)}{2(1+\nu(t))} \quad (2)$$

where $E(t)$ and $\nu(t)$ are the time-dependent Young's modulus and Poisson's ratio, respectively. For predictive modeling, two of the four constants in (2) have to be measured experimentally.

Young's modulus is relatively easy to measure using standard testing apparatuses. There have been several attempts to measure another constant; these include strain gauge [5] and Moiré interferometry [6] for Poisson's ratio measurement, the dilatometer using a fluid pressure [7], [8] for bulk modulus measurement, and dynamic mechanical analyzer (DMA) [9] for shear modulus measurement.

DMA has been most widely used for EMC property measurements. The frequency–temperature sweep can be implemented to measure the temperature- and time-dependent modulus [10]–[12]. Although it is time-consuming, this procedure can be routinely practiced using commercial equipment, but it is usually difficult to obtain elastic constants other than Young's modulus.

Due to the complexity involved in measuring elastic constants other than Young's modulus, it has often been assumed that the bulk modulus is "time-independent" [13]–[15]. This assumption is based on the fact that the viscosity only affects the shear motion of the solid [14]. With this assumption, only Young's modulus has to be measured for viscoelastic modeling. If Poisson's ratio at room temperature (20 °C) is known, the bulk modulus can be approximated as

$$K(t) \approx K = \frac{E(0)|_{T=20\,^\circ\mathrm{C}}}{3(1-2\nu(0)|_{T=20\,^\circ\mathrm{C}})}. \quad (3)$$

It is important to note that the assumption of "time-independent" bulk modulus implies that the bulk modulus becomes temperature-independent if the EMC behavior follows the thermorheological simplicity (TRS) [16], [17]. Using the constant K value, the time-dependent shear modulus can

Manuscript received February 27, 2018; revised May 22, 2018; accepted July 5, 2018. Date of publication July 16, 2018; date of current version August 6, 2018. This work was supported by the Center for Advanced Life Cycle Engineering of the University of Maryland. Recommended for publication by Associate Editor H. Cheng upon evaluation of reviewers' comments. *(Corresponding author: Bongtae Han.)*

The authors are with the Department of Mechanical Engineering, University of Maryland, College Park, MD 20742 USA (e-mail: bthan@umd.edu).

Color versions of one or more of the figures in this paper are available online at http://ieeexplore.ieee.org.

Digital Object Identifier 10.1109/TCPMT.2018.2856249

be calculated as

$$G(t) = \frac{3K \cdot E(t)}{9K - E(t)}. \tag{4}$$

It has been observed that the assumption of a time-independent bulk modulus is not valid for EMC over a wide temperature range [5], [6], [18], [19]. This poses challenges in predicting the warpage of packages at the solder melting temperature, which is much higher than the glass transition temperature of EMC. This issue becomes more critical as the package-on-package (PoP) [20], [21] is more widely used, which is subjected to several reflow cycles during the assembly process.

A fiber Bragg grating (FBG) sensor has been used effectively to characterize the thermomechanical properties of polymers [18], [22]–[26]. In the method, an FBG is embedded at the center of a cylindrical specimen, and it deforms together with the specimen. Then, the properties are determined from the Bragg wavelength (BW) change documented during loading [22], [26].

In this paper, the FBG sensor method is employed to determine the linear viscoelastic properties of EMC. After briefly reviewing the FBG sensor method in Section II, the results obtained from uniaxial compression and hydrostatic pressure are presented in Section III. The validity of three major assumptions associated with the linear viscoelasticity is verified by supplementary experiments in Section IV. The accuracy of the measured properties is corroborated by the warpage measurement in Section V.

II. Background: FBG Sensor Method

The FBG sensor method was originally developed to characterize the curing behavior of advanced semiconductor packaging materials [18], [22]–[25]. More recently, the method was implemented to measure the temperature-dependent elastic properties of EMC [18]. This section reviews the basic concept of the method, the procedure to prepare the EMC specimen, and the test setups for two mechanical loadings—uniaxial compression and hydrostatic pressure.

A. Governing Equation

The specimen configuration and the general loading condition are shown in Fig. 1. An FBG is embedded at the center of a cylindrical-shaped EMC specimen, and the assembly is subjected to an axial pressure P_1 and a radial pressure P_2. An analytical solution for the stress distribution in the fiber and polymer under the generalized plane strain condition is available in the literature, and the detailed description of the solution can be found in [18].

The embedded FBG serves as a strain sensor. The BW shift occurs when the FBG is subjected to stresses. The BW shift and the stress relation can be expressed as [22]

$$\Delta\lambda = \frac{1}{E_f}\left\{\left[1 - \frac{n^2}{2}\left(P_{12} - (P_{12} + P_{11})\nu_f\right)\right]\sigma_{zz}^f - \left[2\nu_f + \frac{n^2}{2}((1-\nu_f)P_{11} + (1-3\nu_f)P_{12})\right]\sigma_{rr}^f\right\}\lambda_i \tag{5}$$

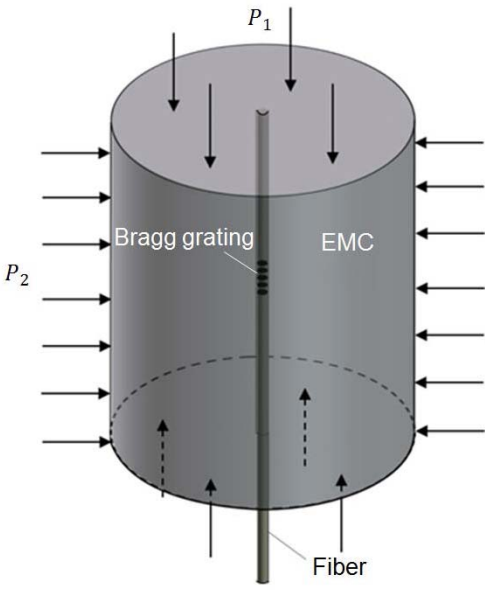

Fig. 1. Specimen configuration and general loading condition.

where $\Delta\lambda$ is the BW shift, λ_i is the initial BW, n is the effective refractive index, and P_{ij} are the strain optic constants [27], [28]. Substituting the stress terms into (5), the BW shift can take the following form [18]:

$$\Delta\lambda = \Pi\left(E_p, \nu_p, \beta\right) \tag{6}$$

where $\beta = (r_p/r_f)$, which is referred to as "configuration," E_p and ν_p are Young's modulus and Poisson's ratio of the polymer, respectively, and Π is a nonlinear function that can be expressed explicitly as a function of the configuration and the properties of polymer and fiber [18].

For a given configuration β, the BW shift is a function of any two of four elastic constants of the polymer. Two constants can be determined from the BW shifts measured from two independent experiments. In order to avoid the complex nonlinear regression with two unknown parameters, a sequential procedure was proposed in [18], where Young's modulus was determined first from the results of uniaxial testing, and the bulk modulus was subsequently determined from the results of hydrostatic pressure testing.

The time-dependent properties can be determined from the BW shift measured as a function of time from the following inverse functions:

$$E_p(t) = \Pi^{-1}(\Delta\lambda(t), \beta), \quad K_p(t) = \Pi^{-1}(\Delta\lambda(t), \beta) \tag{7}$$

where E_p and K_p are Young's modulus and bulk modulus of the polymer, respectively. The descriptions of the inverse functions can be found in [18].

B. EMC Specimen Fabrication

The specimen is fabricated using a custom-designed stainless steel mold assembly, which is shown schematically in Fig. 2 [18]. The inset shows a plunger that applies the required pressure to the specimen. The optical fiber (diameter of 125 μm) is inserted through a small through-hole drilled

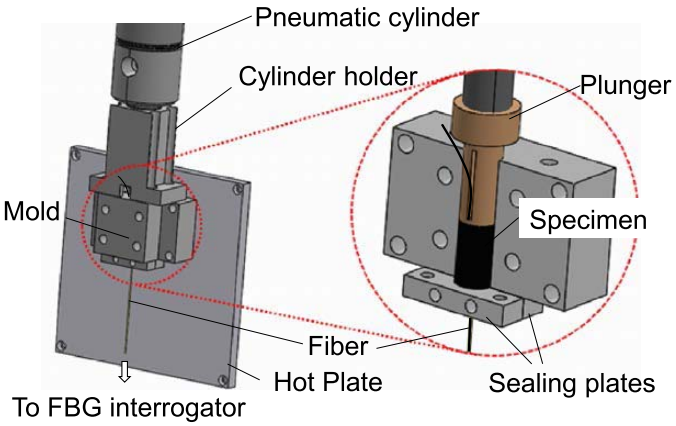

Fig. 2. Mold assembly to fabricate the EMC specimen.

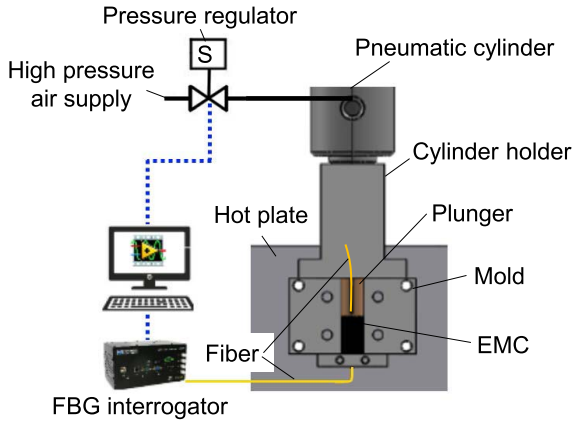

Fig. 3. Setup for specimen fabrication.

in the center of an EMC pellet. The vertical position of the Bragg grating is adjusted until it is placed in the middle of the pellet. The internal surfaces of the mold are treated with a release agent and thermal grease. The pellet is wrapped with a very thin Teflon tape before the curing process starts. This preprocessing ensures easy separation after curing as well as no constraint from the mold walls during curing.

A large mechanical pressure has to be applied during curing. The required pressure (7 MPa) is achieved by the mechanical plunger. As illustrated in Fig. 2 (inset), the plunger is connected to the piston of a pneumatic cylinder. The diameter of the cylinder (31.75 mm) is much larger than the diameter of the plunger (8.9 mm). In this way, the curing pressure is achieved only by an air pressure of 0.54 MPa (78 psi), which is readily available in laboratories.

The complete system is shown in Fig. 3. The mold (with the pellet) is mounted on a high-precision hot/cold plate (HCP304: Instec), which provides temperature control with a resolution of ±0.05 °C. The compressed air line is connected to the pressure regulator (ER3000: Tescom), which is controlled by a PC to produce a desired air pressure to the air cylinder.

After the specimen temperature reaches the curing temperature (175 °C), the curing pressure is applied and maintained during curing. The specimen is released from the mold after 5-min curing time, and it is subsequently subjected to a post-mold curing process (for 2 h at the same temperature without the pressure). More detailed procedure for EMC specimen preparation including the curing pressure application can be found in [18].

C. Uniaxial Compression Test

The uniaxial compression test setup is identical to the one shown in Fig. 2, except that the diameter of the cylindrical chamber is slightly larger than the diameter of the specimen allowing the specimen to deform freely in the radial direction during compressive loading. The maximum pressure provided by the compressed air line is 0.69 MPa (100 psi), and the corresponding maximum compressive loading that the plunger can apply to the specimen is 10.9 MPa.

The specimen and mold subassembly are mounted on the same high-precision hot/cold plate. The bottom end of the fiber is connected to an FBG interrogator (sm125: Micro Optics), and the interrogator is connected to the PC to collect data from the FBG sensor.

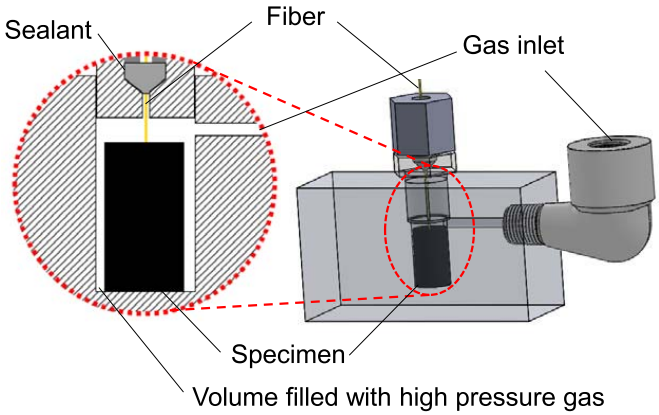

Fig. 4. Setup for the hydrostatic test.

D. Hydrostatic Pressure Test

A higher gas pressure is required for hydrostatic pressure testing simply because it is more difficult to deform the specimen under hydrostatic pressure. A small test chamber is designed to accommodate the required high gas pressure. As shown in Fig. 4, the specimen is placed inside the chamber, which has a slightly larger internal area than the specimen does.

The chamber has to be sealed completely while allowing the fiber to be connected to the interrogator. A special sealing system is used to achieve the requirement. The compressive sealing subassembly is shown schematically in Fig. 5. The fiber passes through the system, which utilizes a deformable (Teflon) sealant to seal the fiber (see the inset of Fig. 5). The chamber is mounted on the same heating stage shown in Fig. 3. The gas inlet of the chamber is connected to a regulator and a helium tank.

The helium tank provides a gas pressure of approximately 15.2 MPa. The output gas from the tank passes through a main regulator (26–2015: Tescom). The main regulator is controlled by a pilot controller (ER3000: Tescom) with a transducer

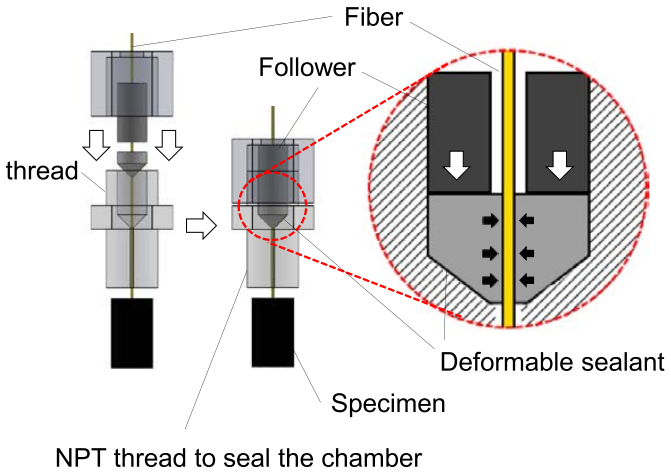

Fig. 5. Compression sealing for the optical fiber.

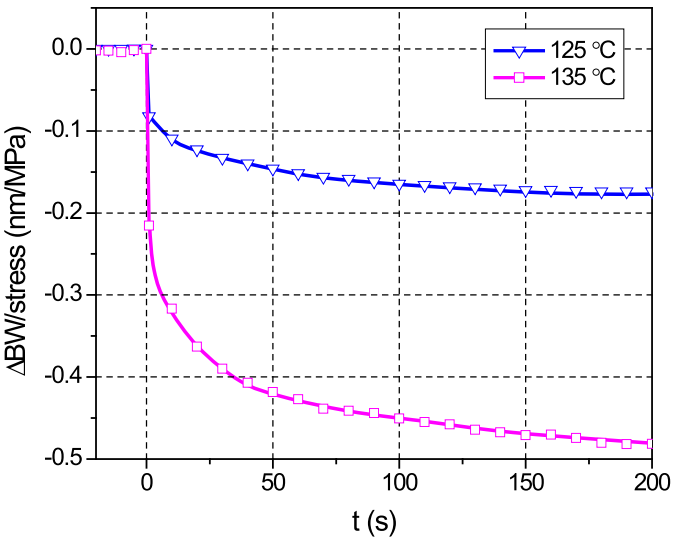

Fig. 6. Normalized BW shift of the compressive creep test at representative temperatures.

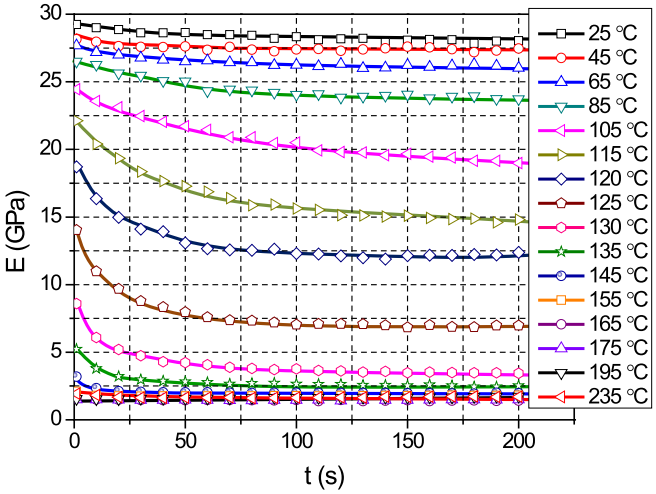

Fig. 7. Relaxation Young's modulus at various temperatures.

(100–1500: Tescom) that provides a feedback to the computer. The output pressure to the test chamber can be controlled with an accuracy of ≈6.9 KPa, and the target pressure is reached within 1 s. The maximum pressure output to the test chamber is 6.9 MPa.

It should be noted that the heat is generated immediately after the target pressure is applied to the test chamber since the gas present (i.e., air) in the chamber is suddenly compressed. This undesired heat causes the thermal expansion of the specimen, which offsets the hydrostatic strain of the specimen. The effect of the heat generation is virtually negated by making the net gas volume smaller than 900 mm^3 [18].

III. Results and Analysis

Two time-dependent properties (Young's modulus and bulk modulus) are presented in Section III-A. The time–temperature superposition is discussed in Section III-B.

A. Relaxation Moduli

The specimen was tested from 25 °C to 235 °C. The temperature interval between measurements was 20 °C below and above the glass transition temperature (130 °C) and 5 °C over the glass transition range. After the first measurement was conducted at room temperature, the mold was heated to the next target temperature. The BW increased with the temperature due to the thermal expansion of the EMC as well as the intrinsic thermal expansion of the fiber. The BW was monitored until it became stabilized. Then, the predetermined loading was applied, and the BW change was recorded as a function of time.

In the uniaxial compression test, three different stresses of 4.98, 1.8, and 0.18 MPa were used for the temperatures below, near, and above the glass transition temperature, respectively, in order to incorporate the strong temperature-dependent initial modulus; the corresponding air cylinder pressures were 344.7, 137.9, 13.8 KPa, respectively.

The representative data obtained from compressive creep testing at two different temperatures are shown in Fig. 6, where the BW changes (ΔBW) are normalized by the applied stresses. The constant BW before loading confirms the temperature stability of the specimen achieved during testing. The initial strains ranged from 50 to 155 $\mu\varepsilon$, and the maximum strains at the end of the tests ranged from 50 to 255 $\mu\varepsilon$.

The relaxation Young's modulus was calculated from the data using (7), and the results are shown in Fig. 7. As expected, Young's modulus changes rapidly with time over the glass transition range. However, at temperatures below and above the glass transition range, Young's modulus has negligible time-dependent behavior.

Creep testing under hydrostatic pressure was conducted at the same temperatures. Two different pressures of 6.9 and 1.4 MPa were applied for the temperatures below and above the glass transition temperature, respectively. The representative data obtained from hydrostatic creep testing at two different temperatures are shown in Fig. 8, where the BW changes (ΔBW) are normalized by the applied stresses. The initial strain ranged from 50 to 140 $\mu\varepsilon$, and the maximum

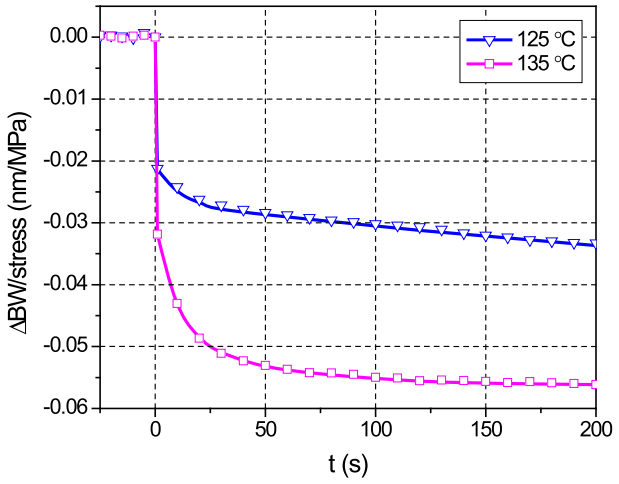

Fig. 8. Normalized BW shift of the hydrostatic creep test at representative temperatures.

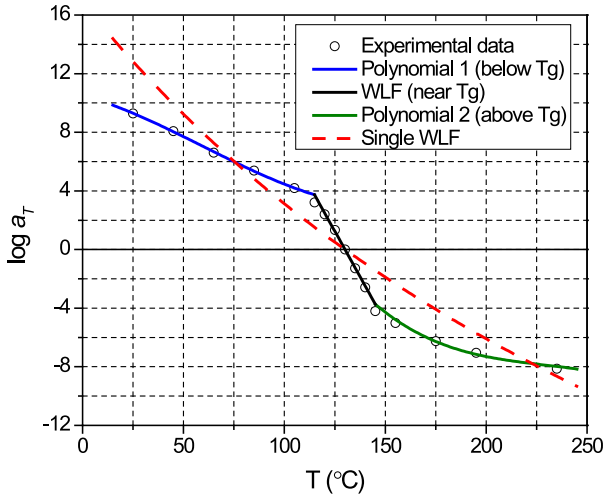

Fig. 10. Shift factors and piecewise shift function.

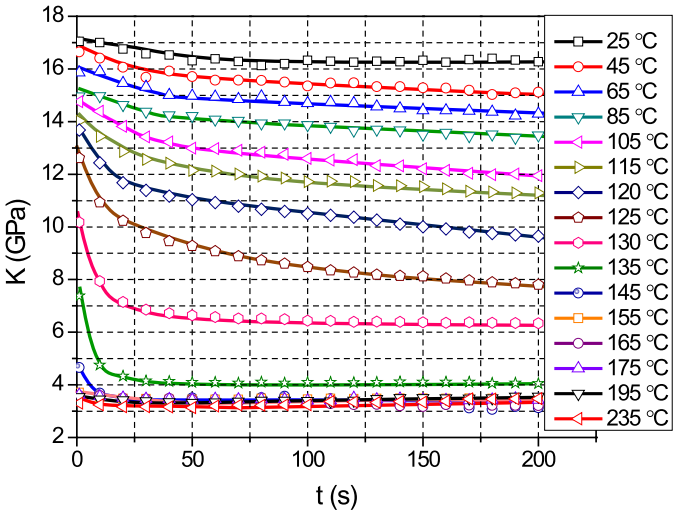

Fig. 9. Time- and temperature-dependent bulk modulus.

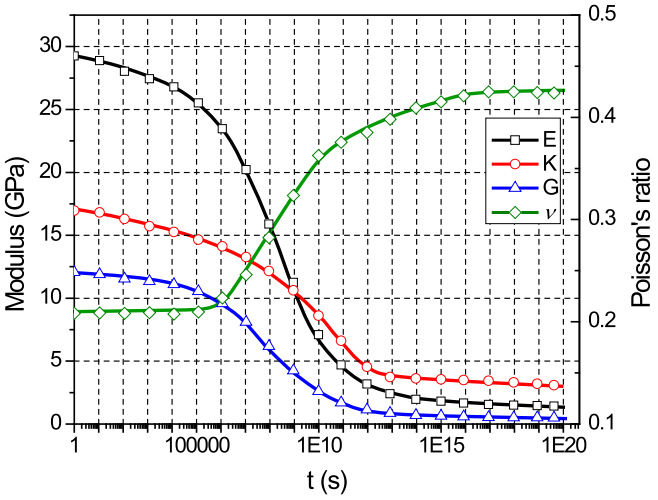

Fig. 11. Master curve of four elastic constants.

stain at the end of the tests was approximately 215 $\mu\varepsilon$. The corresponding relaxation bulk modulus are shown in Fig. 9. A similar time-dependent behavior was observed.

The measurements were repeated at representative temperatures to evaluate the measurement accuracy. The results showed that an accuracy of ± 3 pm was routinely achievable over the temperature range considered in the test, which established some guideline on the accuracy of two properties.

B. Time–Temperature Superposition: Shift Factors

Based on the well-known "TRS" assumption, the time-dependent properties (relaxation moduli) at different temperatures can be shifted and combined using the time–temperature superposition principle [5], [10], [29].

The relaxation Young's modulus obtained at various temperatures was shifted and overlapped to form a master curve of Young's modulus. The shift factors and the master curve of Young's modulus are shown in Figs. 10 and 11, where the reference temperature is 130 °C. Using the same shift factors, the master curve of the bulk modulus was produced, and it is also presented in Fig. 11. The results indicate that the material has only one relaxation mechanism, which confirms the validity of the TRS assumption. The TRS assumption will be validated more quantitatively later.

In the finite-element method (FEM) modeling, the shear modulus and bulk modulus are needed as an input data. The shear modulus can be calculated from Young's modulus and bulk modulus. All three moduli and Poisson's ratio are plotted in Fig. 11. The bulk modulus and shear modulus are fit by the Prony series [5], [10]

$$K(t) = K_\infty + \sum_{i=1}^{20} K_i \exp\left(-\frac{t}{\tau_i}\right)$$
$$G(t) = G_\infty + \sum_{i=1}^{20} G_i \exp\left(-\frac{t}{\tau_i}\right). \quad (8)$$

A single shift function to fit the whole set of shift factors is difficult, especially when a very large temperature range is to be considered. The small discrepancy between the experimentally obtained shift factors and the fit value can cause a large error in the implementation since the time axis of the master curve is in the log scale.

The Williams–Landel–Ferry (WLF) model is the most widely used function for the shift factors [30]. It is based on the free-volume theory; it has been known that the WLF function is more effective for the temperature around T_g [31]–[33].

In this paper, a piecewise shift function is proposed to fit the shift factors. The WLF function is used for the temperatures in the glass transition range. Polynomial functions are used to accommodate the temperatures below and above glass transition temperature. The piecewise shift function can be expressed as

$$\begin{aligned}\log a_T^{p1}(T) &= a_0 + a_1(T-115) + a_2(T-115)^2 \\ &\quad + a_3(T-115)^3 \quad \text{for } T \le 115\ ^\circ\text{C} \\ \log a_T^{\text{WLF}}(T) &= -\frac{C_1(T-130)}{C_2+(T-130)} \quad \text{for } 115\ ^\circ\text{C} \le T \le 145\ ^\circ\text{C} \\ \log a_T^{p2}(T) &= b_0 + b_1(T-145) + b_2(T-145)^2 \\ &\quad + b_3(T-145)^3 \quad \text{for } T \ge 145\ ^\circ\text{C} \end{aligned} \tag{9}$$

where $\log a_T^{p1}$ and $\log a_T^{p2}$ are the polynomial shift functions for the temperatures below and above the glass transition range, respectively, and $\log a_T^{\text{WLF}}$ is the WLF function for the temperatures of the glass transition range. It is to be noted that $a_0 = \log a_T^{\text{WLF}}(115)$ and $b_0 = \log a_T^{\text{WLF}}(145)$, which makes the piecewise shift function continuous. The function is empirical but can accommodate more than one temperature range. The constants of (9) are

$$\begin{aligned} &a_1 = -4.18\cdot 10^{-2};\quad a_2 = 4.87\cdot 10^{-4};\ a_3 = 2.94\cdot 10^{-6} \\ &C_1 = 3.71\cdot 10^{3};\quad C_2 = 1.49\cdot 10^{4} \\ &b_1 = -1.17\cdot 10^{-1};\quad b_2 = 1.20\cdot 10^{-3};\ b_3 = -4.78\cdot 10^{-6}. \end{aligned}$$

The results of the piecewise shift function are shown in Fig. 10. The shift factors over the entire temperature range are represented accurately by the piecewise shift function. A single WLF function that represents the entire shift factors is also shown in Fig. 10. It is evident that a single WLF function should not be used for the entire temperature range. Otherwise, it would be prone to large errors in shift factor calculations.

IV. Validity of Linear Viscoelasticity

The validity of three major assumptions associated with the linear viscoelasticity is verified by supplementary experiments. The assumptions to be examined include TRS, Boltzmann superposition, and linearity.

A. Thermorheological Simplicity

The time–temperature superposition process is based on the TRS [34]. The assumption states that the shapes of the master curve are the same in the log-time scale at different temperatures. This assumption is not always valid for polymeric materials [35], [36]. An extra long-term creep test was conducted to verify the validity of the assumption.

The long-term test was conducted at 125 °C for approximately 4 h. The temperature was chosen to obtain the strong viscoelastic behavior. The raw data of the long-term test are shown in Fig. 12(a). The time-dependent Young's modulus obtained from the long-term creep test is plotted in the log-time scale, and it is compared with the master curve in Fig. 12(b). The long-term creep data overlaps with the master curve very well, which confirms that the TRS assumption is valid for the EMC material tested in the study.

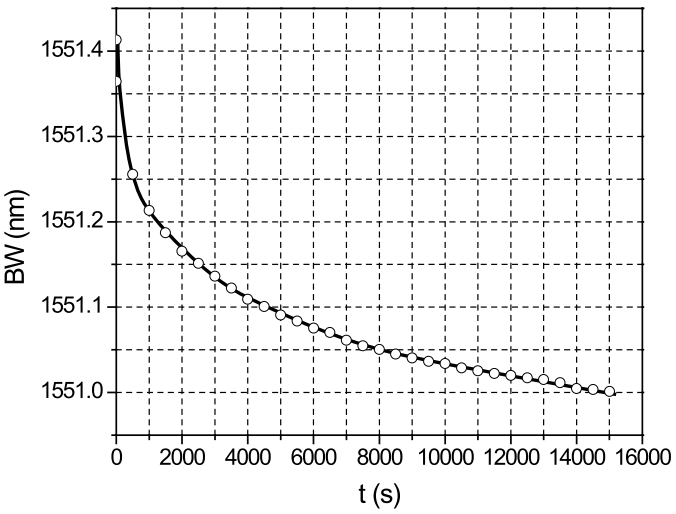

(a)

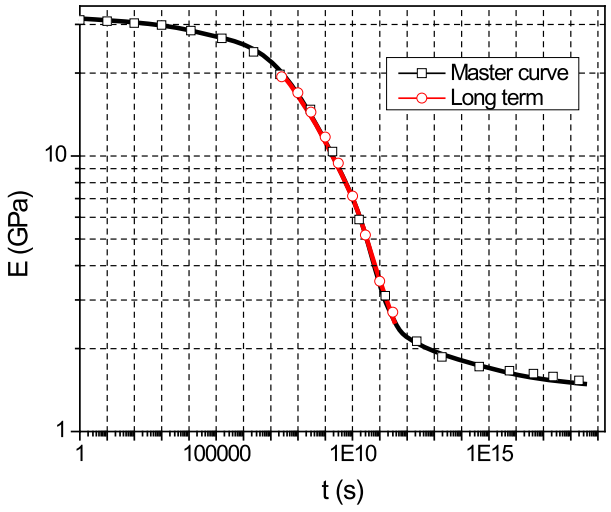

(b)

Fig. 12. (a) Raw data of a long-term test at 125 °C. (b) Comparison with the master curve in the log-time scale.

B. Boltzmann Superposition Principle

The Boltzmann superposition principle (BSP) states that "in the linear viscoelastic regime, the strain response to successive stress is additive" [37]. It is the key to develop the linear viscoelastic constitutive law. In order to verify its validity, a supplementary experiment was conducted at 130 °C with a two-step loading. An initial loading of 0.07 MPa was applied at $t = 0$, and an additional loading of 0.07 MPa was applied suddenly at $t = 100$ s. The BW change measured during the whole process was documented.

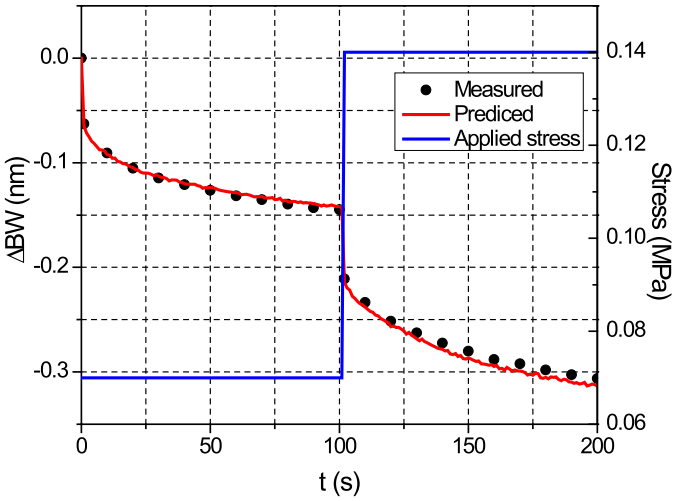

Fig. 13. Supplementary experiment to verify BSP.

Based on the BSP, the strain change due to the step loading can be calculated from the following equation:

$$\varepsilon(t) = J(t) \cdot \sigma + J(t-\tau) \cdot \Delta\sigma \tag{10}$$

where $\varepsilon(t)$ is the strain change as a function of time, $J(t)$ is the time-dependent compliance, which can be determined from the time-dependent Young's modulus, σ is the applied stresses, and $\Delta\sigma$ is the stress increment.

The BW change under the same loading condition can be calculated from the strain $\varepsilon(t)$. The measured BW changes are compared with the predicted values in Fig. 13. The measured values match very well with the predicted values, indicating the validity of the BSP for the material.

C. Strain-Independent Relaxation Modulus

In the domain of linear viscoelasticity, the time-dependent (or relaxation) modulus should be independent of the applied stress (or strain) level. Three independent tests were conducted at 120 °C to verify the validity. The BW changes obtained from three applied stresses (0.5, 1, and 2 MPa) are shown in Fig. 14(a).

The relaxation modulus is calculated from the BW, and they are shown in Fig. 14(b). It is evident that the relaxation modulus is independent of the applied stresses, confirming that the linear viscoelasticity is valid for the material. It is worth noting that the maximum strain level applied during this test was smaller than 400 $\mu\varepsilon$, which ensured that the tests were conducted within the linear viscoelasticity domain.

V. Verification of Numerical Modeling Approach

A. Shift Factors and Prony Series

The user-defined subroutine was developed to accommodate the piecewise shift function in ANSYS. A unit stress was applied to the model at a given temperature, and the modulus was determined from the strain response predicted by the FEM model.

The predicted Young's modulus and bulk modulus at four different temperatures (below the glass transition, within the glass transition, and above the glass transition) are compared with the experimental data in Fig. 15. The plot shows a very good agreement between the predicted results and the experimental data, confirming that the measured properties are accurately represented by the master curve and the shift functions.

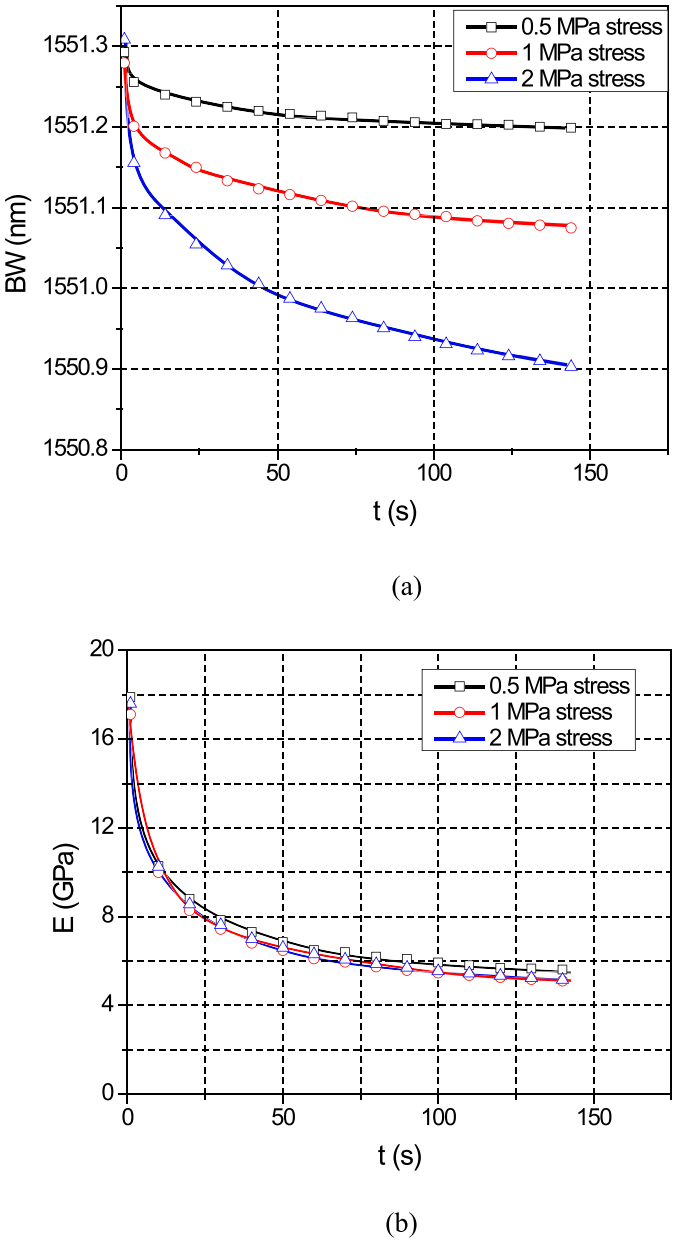

(a)

(b)

Fig. 14. Time-dependent behavior at different stress levels. (a) BW. (b) Young's modulus.

B. Experimental Verification

The bimaterial specimen with a layer of the silicon chip and EMC is used for the warpage measurement at different temperatures [Fig. 16(a)]. The width and length of the specimen are 2 and 20 mm, respectively, and the thicknesses of the EMC and the chip are 0.2 and 0.6 mm, respectively.

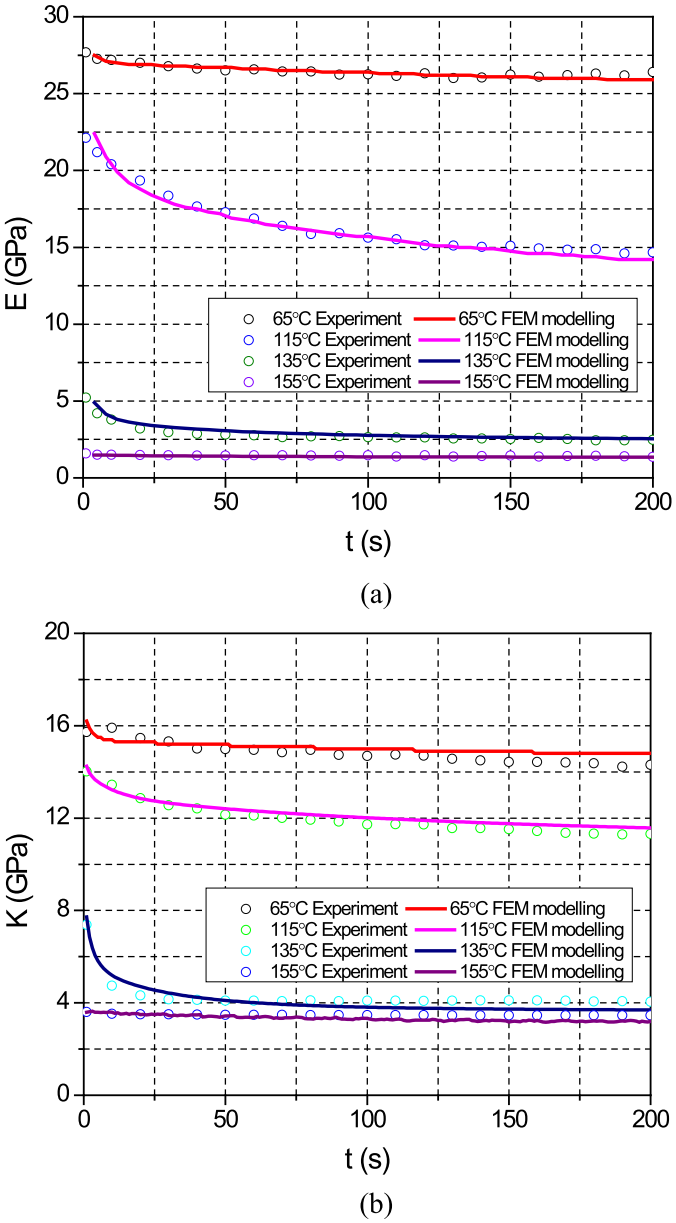

Fig. 15. Comparison between the prediction and experimental data. (a) Young's modulus. (b) Bulk modulus.

Twyman–Green (T/G) interferometry is a classical interferometry, which utilizes the interference of coherent light to document the surface topography of a specular surface [38]. The optical setup used in the paper is illustrated in Fig. 16(b). A coherent light source (usually a laser) is collimated by a collimating lens and then passes through a beam splitter. The beams from the reference path (the mirror) and the active path (the specimen) are combined to produce a fringe pattern seen by the camera. The fringe pattern represents the contour map of out-of-plane displacement (or warpage). With this configuration, the warpage of the bimaterial W can be determined by

$$W = \frac{N}{2}\lambda \tag{11}$$

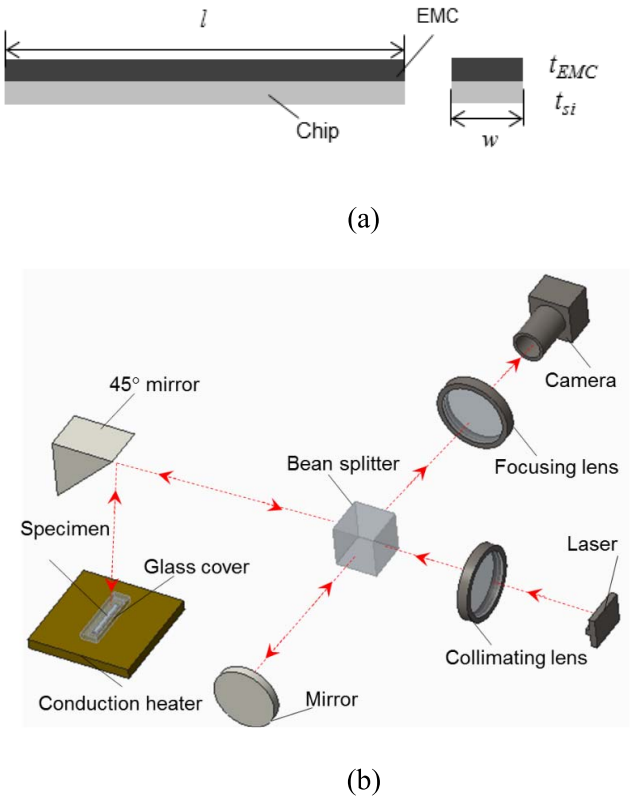

Fig. 16. (a) Bimaterial specimen. (b) T/G interferometry setup for warpage measurement.

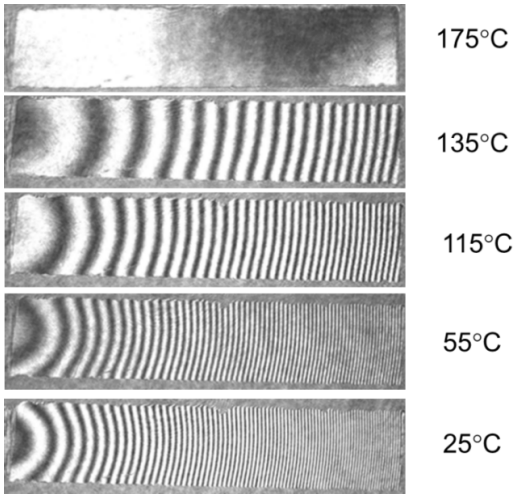

Fig. 17. Temperature-dependent fringes.

where N is the order of fringes, and λ is the wavelength of the laser. A He–Ne laser with $\lambda = 633$ nm was employed in the experiment, and the contour interval was 0.316 μm/fringe.

The specimen was placed on the conduction heater covered by a small glass chamber to eliminate the air flow. The specimen was cooled from 175 °C (EMC curing temperature) to 25 °C with a cooling rate of 20 °C/min. A thermocouple was attached to the heater close to the specimen to accurately monitor the specimen temperature. The representative fringe patterns of the right half of the specimen, obtained at 175 °C, 135 °C, 115 °C, 55 °C, and 25 °C, are shown in Fig. 17.

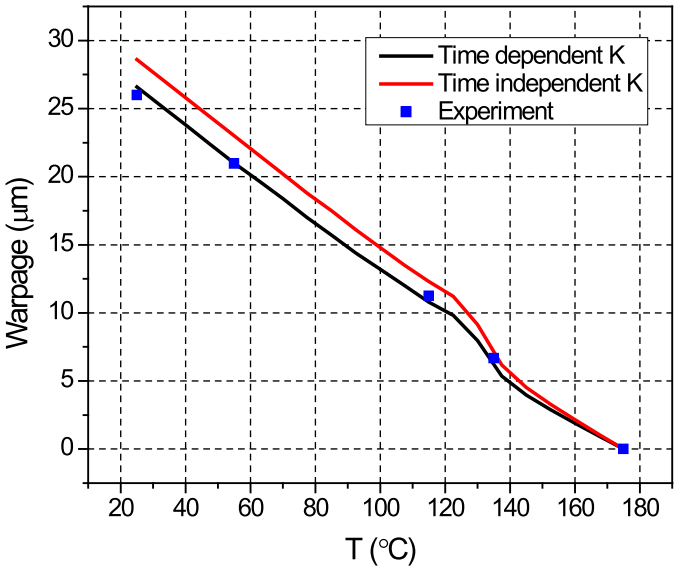

Fig. 18. Warpage comparison between FEM and experiment.

An FEM model was created to verify the viscoelastic behavior of the material. The coefficient of thermal expansion (CTE) of the EMC was measured separately by thermomechanical analyzer: CTE below and above T_g were 8 and 40 ppm/°C, respectively. The input properties for the chip were $E_{si} = 112$ GPa, $\nu_{si} = 0.28$, $\text{CTE}_{si} = 2.6$ ppm/°C. The same temperature loading (cooling from 175 °C with a cooling rate of 20 °C/min) was applied to the model.

The results are compared in Fig. 18. The numerical predictions match very well to the experimental data, corroborating the validity of the measured properties. The model prediction using the time-independent bulk modulus was also conducted. The results indicate that the time-impendent bulk modulus assumption overestimated the warpage at room temperature approximately by 15%.

VI. Conclusion

Two linear viscoelastic properties of an EMC material were measured by the FBG-based method from a single cylindrical specimen configuration. The EMC specimen was subjected to constant uniaxial compression and hydrostatic pressure at various temperatures. Two master curves of Young's modulus and bulk modulus, as well as the corresponding shift factors, were determined from the experimental data. The validity of three major assumptions associated with the linear viscoelasticity was verified quantitatively. The results showed that the linear viscoelasticity described the behavior of the EMC very well as long as the maximum strain was in the linear domain. The measured properties were also verified by using the warpage data obtained from of a bimaterial specimen subjected to a temperature cycle. The results corroborated the accuracy of the measured properties.

References

[1] W. Tan, F. Zhou, X. Cheng, D. Ding, and J. Wu, "The warpage control method in epoxy molding compound," in *Proc. Int. Conf. Electron. Packag. Technol. High Density Packag. (ICEPT-HDP)*, Aug. 2009, pp. 722–724.

[2] Y. L. Tzeng, N. Kao, E. Chen, J. Y. Lai, Y. P. Wang, and C. S. Hsiao, "Warpage and stress characteristic analyses on package-on-package (POP) structure," in *Proc. 9th Electron. Packag. Technol. Conf. (EPTC)*, Dec. 2007, pp. 482–487.

[3] W. H. Zhu *et al.*, "Cure shrinkage characterization and its implementation into correlation of warpage between simulation and measurement," in *Proc. Int. Conf. Thermal, Mech. Multi-Phys. Simulation Exp. Microelectron. Micro-Syst. (EuroSime)*, Apr. 2007, pp. 1–8.

[4] A. V. Amirkhizi, J. Isaacs, J. McGee, and S. Nemat-Nasser, "An experimentally-based viscoelastic constitutive model for polyurea, including pressure and temperature effects," *Philos. Mag.*, vol. 86, no. 36, pp. 5847–5866, 2006.

[5] L. J. Ernst, G. Q. Zhang, K. M. B. Jansen, and H. J. L. Bressers, "Time-and temperature-dependent thermo-mechanical modeling of a packaging molding compound and its effect on packaging process stresses," *J. Electron. Packag.*, vol. 125, pp. 539–548, Dec. 2003.

[6] D. J. O'Brien, N. R. Sottos, and S. R. White, "Cure-dependent viscoelastic Poisson's ratio of epoxy," *Exp. Mech.*, vol. 47, pp. 237–249, Apr. 2007.

[7] M. Sadeghinia, K. M. B. Jansen, and L. J. Ernst, "Characterization and modeling the thermo-mechanical cure-dependent properties of epoxy molding compound," *Int. J. Adhes. Adhesives*, vol. 32, pp. 82–88, Jan. 2012.

[8] I. Emri and T. Prodan, "A measuring system for bulk and shear characterization of polymers," *Exp. Mech.*, vol. 46, pp. 429–439, Aug. 2006.

[9] W. D. van Driel, J. H. J. Janssen, G. Q. Zhang, D. G. Yang, and L. J. Ernst, "Packaging induced die stresses—Effect of chip anisotropy and time-dependent behavior of a molding compound," *J. Electron. Packag.*, vol. 125, pp. 520–526, Dec. 2003.

[10] S.-H. Chae, J.-H. Zhao, D. R. Edwards, and P. S. Ho, "Characterization of viscoelasticity of molding compounds in time domain," in *Proc. ASME InterPACK Conf. Collocated ASME Summer Heat Transf. Conf., 3rd Int. Conf. Energy Sustain.*, 2009, pp. 435–441.

[11] J. Z. Liang, R. K. Y. Li, and S. C. Tjong, "Effects of glass bead size and content on the viscoelasticity of filled polypropylene composites," *Polym. Test.*, vol. 19, pp. 213–220, Apr. 2000.

[12] R. Hagen, L. Salmén, H. Lavebratt, and B. Stenberg, "Comparison of dynamic mechanical measurements and T_g determinations with two different instruments," *Polym. Test.*, vol. 13, no. 2, pp. 113–128, 1994.

[13] D.-L. Chen, P.-F. Yang, and Y.-S. Lai, "A review of three-dimensional viscoelastic models with an application to viscoelasticity characterization using nanoindentation," *Microelectron. Rel.*, vol. 52, pp. 541–558, Mar. 2012.

[14] H. F. Brinson and L. C. Brinson, *Polymer Engineering Science and Viscoelasticity*. New York, NY, USA: Springer, 2008.

[15] J. de Vreugd *et al.*, "Advanced viscoelastic material model for predicting warpage of a QFN panel," in *Proc. 58th Electron. Compon. Technol. Conf. (ECTC)*, May 2008, pp. 1635–1640.

[16] R. D. Maksimov and É. Z. Plume, "Predicting the creep of unidirectional reinforced plastic with thermorheologically simple structural components," *Mech. Compos. Mater.*, vol. 18, pp. 737–744, Nov. 1983.

[17] A. Sarhadi, J. H. Hattel, and H. N. Hansen, "Precision glass molding: Validation of an FE model for thermo-mechanical simulation," *Int. J. Appl. Glass Sci.*, vol. 5, pp. 297–312, Sep. 2014.

[18] Y. Sun, H.-S. Lee, and B. Han, "Measurement of elastic properties of epoxy molding compound by single cylindrical configuration with embedded fiber Bragg grating sensor," *Exp. Mech.*, vol. 57, pp. 313–324, Feb. 2017.

[19] P. J. Gromala, A. Prisacaru, M. Jeronimo, H.-S. Lee, Y. Sun, and B. Han, "Non-linear viscoelastic modeling of epoxy based molding compound for large deformations encountered in power modules," in *Proc. IEEE 67th Electron. Compon. Technol. Conf. (ECTC)*, May/Jun. 2017, pp. 834–840.

[20] A. Yoshida *et al.*, "A study on package stacking process for package-on-package (PoP)," in *Proc. 56th Electron. Compon. Technol. Conf.*, May/Jun. 2006, p. 6.

[21] N. Vijayaragavan, F. Carson, and A. Mistry, "Package on package warpage—Impact on surface mount yields and board level reliability," in *Proc. 58th Electron. Compon. Technol. Conf. (ECTC)*, May 2008, pp. 389–396.

[22] Y. Wang, L. Woodworth, and B. Han, "Simultaneous measurement of effective chemical shrinkage and modulus evolutions during polymerization," *Exp. Mech.*, vol. 51, pp. 1155–1169, Sep. 2011.

[23] Y. Sun, Y. Wang, C. Jang, B. Han, and K. Y. Choi, "Generalized hybrid modeling to determine chemical shrinkage and modulus evolutions at arbitrary temperatures," *Exp. Mech.*, vol. 53, pp. 1783–1790, Nov. 2013.

[24] Y. Sun, Y. Wang, Y. Kim, and B. Han, "Dual-configuration fiber Bragg grating sensor technique to measure coefficients of thermal expansion and hygroscopic swelling," *Exp. Mech.*, vol. 54, pp. 593–603, Apr. 2014.
[25] Y. Sun, B. Han, E. Parsa, and A. Dasgupta, "Measurement of effective chemical shrinkage and equilibrium modulus of silicone elastomer used in potted electronic system," *J. Mater. Sci.*, vol. 49, pp. 8301–8310, Dec. 2014.
[26] D. Karalekas, J. Cugnoni, and J. Botsis, "Monitoring of process induced strains in a single fibre composite using FBG sensor: A methodological study," *Compos. A, Appl. Sci. Manuf.*, vol. 39, pp. 1118–1127, Jul. 2008.
[27] N. Tanaka, Y. Okabe, and N. Takeda, "Temperature-compensated strain measurement using fiber Bragg grating sensors embedded in composite laminates," *Smart Mater. Struct.*, vol. 12, no. 6, p. 940, 2003.
[28] X. Tao, L. Tang, W.-C. Du, and C.-L. Choy, "RETRACTED: Internal strain measurement by fiber Bragg grating sensors in textile composites," *Compos. Sci. Technol.*, vol. 60, pp. 657–669, Apr. 2000.
[29] N. Srikanth, "Warpage analysis of epoxy molded packages using viscoelastic based model," *J. Mater. Sci.*, vol. 41, pp. 3773–3780, Jun. 2006.
[30] M. L. Williams, R. F. Landel, and J. D. Ferry, "The temperature dependence of relaxation mechanisms in amorphous polymers and other glass-forming liquids," *J. Amer. Chem. Soc.*, vol. 77, no. 14, pp. 3701–3707, 1955.
[31] P. Sopade, P. Halley, B. Bhandari, B. D'Arcy, C. Doebler, and N. Caffin, "Application of the Williams–Landel–Ferry model to the viscosity–temperature relationship of Australian honeys," *J. Food Eng.*, vol. 56, pp. 67–75, Jan. 2003.
[32] D. J. Pooler, "The temperature dependent non-linear response of a wood plastic composite," Ph.D. dissertation, School Mater. Mech. Eng., Washington State Univ., Pullman, WA, USA, 2001.
[33] F. R. Schwarzl and F. Zahradnik, "The time temperature position of the glass-rubber transition of amorphous polymers and the free volume," *Rheologica Acta*, vol. 19, pp. 137–152, Mar. 1980.
[34] A. D. Drozdov, *Mechanics of Viscoelastic Solids*. Hoboken, NJ, USA: Wiley, 1998.
[35] L. G. Brinson and W. G. Knauss, "Thermorheologically complex behavior of multi-phase viscoelastic materials," *J. Mech. Phys. Solids*, vol. 39, no. 7, pp. 859–880, 1991.
[36] E. T. J. Klompen and L. E. Govaert, "Nonlinear viscoelastic behaviour of thermorheologically complex materials," *Mech. Time-Dependent Mater.*, vol. 3, pp. 49–69, Mar. 1999.
[37] W. N. Findley and J. S. Y. Lai, "A modified superposition principle applied to creep of nonlinear viscoelastic material under abrupt changes in state of combined stress," *Trans. Soc. Rheol.*, vol. 11, no. 3, pp. 361–380, 1967.
[38] D. Post, B. Han, and P. Ifju, *High Sensitivity Moiré: Experimental Analysis for Mechanics and Materials* (Mechanical Engineering Series). New York, NY, USA: Springer, 1994.

Hyun Seop Lee received the B.S. degree in mechanical engineering from Sungkyunkwan University, Suwon, South Korea, in 2014. He is currently pursuing the Ph.D. degree in mechanical engineering with the University of Maryland at College Park, College Park, MD, USA.

His current research interests include characterization of polymers for advanced packaging, electronic packaging, and reliability.

Yong Sun received the Ph.D. degree in mechanical engineering from the University of Maryland at College Park, College Park, MD, USA, in 2016.

After that, he joined industry as a Hardware Engineer.

Changsu Kim received the B.Sc. degree in mechanical engineering from Hanyang University, Seoul, South Korea, in 2015, and the M.Sc. degree in mechanical engineering from New York University, New York, NY, USA, in 2017. He is currently pursuing the Ph.D. degree in mechanical engineering with the University of Maryland at College Park, College Park, MD, USA.

His doctoral research focuses on characterizations of semiconductor packaging materials.

Bongtae Han received the B.S. and M.S. degrees in mineral and petroleum engineering from Seoul National University, Seoul, South Korea, in 1981 and 1983, respectively, and the Ph.D. degree in engineering mechanics from Virginia Tech, Blacksburg, VA, USA, in 1991.

He is a Keystone Professor of Engineering currently directing the Laboratory for Optomechanics and Micro/nano Semiconductor/Photonics Systems, Center for Advanced Life Cycle Engineering, University of Maryland at College Park, College Park, MD, USA.

Dr. Han served as an Associate Technical Editor for *Experimental Mechanics* from 1999 to 2001, and the *Journal of Electronic Packaging* from 2003 to 2012. He is currently serving as an Associate Editor for *Microelectronics Reliability*. He was elected a fellow of the SEM and the ASME in 2006 and 2007, respectively.